Article

Characterization of a Transmon Qubit in a 3D Cavity for Quantum Machine Learning and Photon Counting

Alessandro D'Elia [1],*, Boulos Alfakes [2], Anas Alkhazaleh [2], Leonardo Banchi [3,4], Matteo Beretta [1], Stefano Carrazza [2,5,6,7], Fabio Chiarello [1,8], Daniele Di Gioacchino [1], Andrea Giachero [9,10,11], Felix Henrich [12], Alex Stephane Piedjou Komnang [1], Carlo Ligi [1], Giovanni Maccarrone [1], Massimo Macucci [13], Emanuele Palumbo [9,10], Andrea Pasquale [2,5,6], Luca Piersanti [1], Florent Ravaux [2], Alessio Rettaroli [1], Matteo Robbiati [5,7], Simone Tocci [1] and Claudio Gatti [1]

1   INFN—Laboratori Nazionali di Frascati, 00044 Frascati, Italy; matteo.beretta@lnf.infn.it (M.B.); fabio.chiarello@ifn.cnr.it (F.C.); apiedjou@lnf.infn.it (A.S.P.K.); carlo.ligi@lnf.infn.it (C.L.); giovanni.maccarrone@lnf.infn.it (G.M.); luca.piersanti@lnf.infn.it (L.P.); alessio.rettaroli@lnf.infn.it (A.R.); simone.tocci@lnf.infn.it (S.T.); claudio.gatti@lnf.infn.it (C.G.)
2   Quantum Research Centre, Technology Innovation Institute, Abu Dhabi P.O. Box 9639, United Arab Emirates; boulos.alfakes@tii.ae (B.A.); anas.alkhazaleh@tii.ae (A.A.); stefano.carrazza@cern.ch (S.C.); andrea.pasquale@unimi.it (A.P.); florent.ravaux@tii.ea (F.R.)
3   Dipartimento di Fisica e Astronomia, Universita di Firenze, 50019 Sesto Fiorentino, Italy; leonardo.banchi@unifi.it
4   INFN—Sezione di Firenze, 50019 Sesto Fiorentino, Italy
5   TIF Lab, Dipartimento di Fisica, Università degli Studi di Milano, 20133 Milano, Italy; matteo.robbiati@cern.ch
6   INFN Sezione di Milano, Via Giovanni Celoria 16, 20133 Milan, Italy
7   CERN, Theoretical Physics Department, CH-1211 Geneva, Switzerland
8   Istituto di Fotonica e Nanotecnologie CNR, 00156 Roma, Italy
9   Dipartimento di Fisica, Università di Milano-Bicocca, 20126 Milano, Italy; andrea.giachero@mib.infn.it (A.G.); emanuele.palumbo@lnf.infn.it (E.P.)
10 INFN Sezione di Milano Bicocca, Piazza della Scienza 3, 20126 Milano, Italy
11 Bicocca Quantum Technologies (BiQuTe) Centre, 20126 Milano, Italy
12 Departement of Physics and Astronomy, University of Heidelberg, 69120 Heidelberg, Germany; felix.henrich@stud.uni-heidelberg.de
13 Dipartimento di Ingegneria dell'Informazione, Università di Pisa, Via G. Caruso 16, 56122 Pisa, Italy; massimo@mercurio.iet.unipi.it
*   Correspondence: alessandro.delia@lnf.infn.it

Abstract: In this paper, we report the use of a superconducting transmon qubit in a 3D cavity for quantum machine learning and photon counting applications. We first describe the realization and characterization of a transmon qubit coupled to a 3D resonator, providing a detailed description of the simulation framework and of the experimental measurement of important parameters, such as the dispersive shift and the qubit anharmonicity. We then report on a Quantum Machine Learning application implemented on a single-qubit device to fit the u-quark parton distribution function of the proton. In the final section of the manuscript, we present a new microwave photon detection scheme based on two qubits coupled to the same 3D resonator. This could in principle decrease the dark count rate, favoring applications like axion dark matter searches.

Keywords: transmon; qubit characterization; transmon simulation; microwave photon detection

1. Introduction

Quantum computation is nowadays one of the most attractive areas of research. The main advantage of quantum computation over classical computation resides in the qubit as the quantum equivalent of the binary logical bit [1]. Among the many qubit types, superconducting qubits based on Josephson junctions (JJs) are the most promising since they can be printed on substrates like silicon electronics, retaining great scalability potential [2].

JJs are versatile superconducting devices that can be used for many cutting edge applications such as microwave photon detection [3–10], parametric amplification [11–13], and entangled photon emission [14–16]. The JJ is described formally by a fictitious phase particle trapped in a slightly anharmonic potential well. The first two energy levels can be used as a two-level system, i.e., a qubit [17].

The most diffuse superconducting qubit is the transmon because of its simple design and solid performance. The transmon is composed of a small JJ shunted by large capacitors to minimize the charge noise [18]. The best transmon performances in terms of coherence time now approach 500 μs [19]. Different designs have been proposed to exceed transmon performances, including the $0–\pi$ qubit, the fluxonium, or the unimon [20–22]. However, they usually have much more complex circuits or control schemes with respect to the transmon and a net superiority has not been established yet. Because of the relevance of the transmon, its design and characterization are of crucial importance in the field of quantum technologies to enable qubit-based pioneering applications.

In this paper, we report the use of a superconducting transmon qubit in a 3D cavity for quantum machine learning and photon detection applications. Notably, 3D architectures have several advantages in particular for those applications such as photon detection that do not require a large number of qubits. Dielectrics surfaces are in fact generally much lossier than bulk cavities. Al cavities reach up to 10 ms photon lifetime independent of the stored power and down to the single photon level [23]. Superconducting qubits hosted in a 3D cavity recorded coherence time T_2 above 1 ms [24]. Moreover, superconducting microwave cavities coupled to one or more anharmonic elements in the circuit quantum electrodynamics architecture are today explored for hardware-efficient encoding of logical qubits [25].

The paper will develop as follows: In Section 2, the transmon fabrication method and the experimental setup are described. In Section 3, we show the spectroscopic and time domain characterization of our transmon. In Section 4, we discuss the simulation framework necessary to design a transmon with the desired properties. In Section 5, as a quantum machine learning application, we report the fit to the u-quark Parton Distribution Function of the proton with the superconducting qubit device. Finally, in Section 6, we describe a new measurement protocol for a low dark-count photon detector with two qubits.

2. Materials and Methods

2.1. Transmon Fabrication

The device was fabricated at the Technology Innovation Institute in Masdar City, Abu Dhabi. A high resistivity (>20 kΩ·cm) (100) FZ silicon was used. The wafer was diced into square pieces of 22 mm × 22 mm with half cuts (from the backside of the wafer) of 2 mm × 14 mm as the cavity slot dimensions. Those half-cuts allow manual cleaving post junction fabrication, avoiding exposing the junction for a protective resist layer if dicing was to be performed afterwards. Dies were sonicated in Acetone and IPA for 5 min.

A bilayer stack of resist was spun using a SCS 6808 spin coater (Indianapolis, IN, USA). In total, 500 nm of Kayaku PMGI SF9 (Westborough, MA, USA) was used for the bottom layer and 200 nm of Allresist GmbH AR-P 6200.9 (CSAR) (Strausberg, Germany) was used for the top layer. Both the shunting capacitors and the junctions were written using a Raith eLINE Plus electron beam lithography system. In total, 20 keV, an aperture of 60 μm, and a dose of 185 μC/cm^2 was used for the capacitors, while the junctions were written with a smaller 15 μm aperture and a dose of 112.5 μC/cm^2. Post exposure, the samples were developed using Allresist AR 600-546 and Kayaku diluted 101A for the top and bottom layers, respectively.

Subsequently, the dies were loaded into a Plassys MEB 550s (Marolles-en-Hurepoix, Freance) e-beam evaporation system. The system was allowed to pump to below 9×10^{-8} mbar of pressure. The evaporation was performed at a 55° tilt angle using the Manhattan approach. In total, 35 nm of Al were deposited at a rate of 0.6 nm/s, followed by a static oxidation at 0.625 mbar for 25 min, and a second Al evaporation of 55 nm.

Liftoff was performed in a bath of N-Methylpyrrolidone at 70 °C. A test structure on the same die was used to measure room temperature resistance using a S-1160 manual probe station from Signatone (Gilroy, CA, USA) and a 2450 SMU from Keithley (Cleveland, OH, USA). In total, $4849 \pm 115\ \Omega$ was measured for the device used in this work. An optical image of the transmon chip within the resonator and of the device is shown in Figure 1. The junction area is roughly $200 \times 200\ \text{nm}^2$ and the two antenna pads separated by 20 μm are 556 μm long and 144 μm wide.
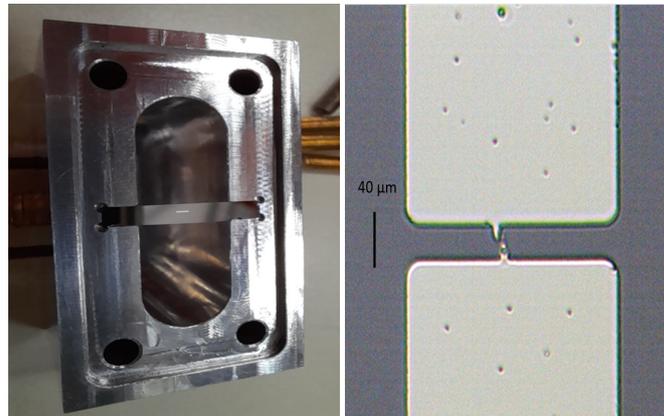
Figure 1. (**Left**): Al cavity hosting the transmon chip. (**Right**): optical image of the transmon shunt capacitance pads acquired with a 100× magnification. The JJ is not observable since it is roughly $200 \times 200\ \text{nm}^2$, but it is located between the pads, in proximity of the two observable metal extensions.

The resonant cavity is made of Al alloy 6061 with a rectangular parallelepiped shape of dimensions $L_x \times L_y \times L_z = 26 \times 36 \times 8\ \text{mm}^3$. The silicon chip with the qubits is hosted in the middle of the $x - y$ plane with pads parallel to the z axis (see Section 4) to couple to the mode TE110. Two holes allow for the insertion of the antennas for control and readout of the qubit state.

2.2. Experimental Setup for Transmon Characterization

Full characterization of the 3D transmon qubit was performed at the INFN National Laboratory of Frascati. The experimental setup is shown in Figure 2.

The dashed lines indicate the different temperature stages of the cryostat of a dilution refrigerator. The device is hosted in the 10 mK stage. Control and readout signals entering Line 1 are attenuated by -20 dB at 4 K and by -30 dB at 10 mK. Including the attenuation of the coaxial cable, the total attenuation is -68 dB.

Both input and output ports are filtered with IR and low-pass filters with a 10 GHz cut-off frequency, while an additional 4 GHz high-pass filter is mounted on the input port. The output signal passing through Line 5 is amplified with a high electron mobility transistor by 36 dB at 4 K and with two field effect transistors by 35 db and 30 dB at 300 K. Two circulators are used to minimize the reflected noise and decouple the amplification stages.

For time-domain measurements, the qubit control pulses are directly produced by a RF source (ROHDE-SCHWARZ SMA100B). The readout pulse is obtained by the vector modulation of a signal generated by a second RF source (ROHDE-SCHWARZ SGS100A) at the cavity frequency and controlled by a square-wave pulse a width of 10 μs generated by a wave function generator (KEYSIGHT 33500B) triggered by the SMA100B.

Both the control and readout pulses are transmitted to Line 1 through a combiner. After amplification, the readout pulse is down-converted and I and Q quadratures are acquired with a 16-bit ADC board at a rate of 1 GS/s and post-processed to determine the qubit state.

For cavity and qubit spectroscopy, the generation and acquisition of the readout pulse is replaced by the S21 measurement with Vector Network Analyzer (VNA).
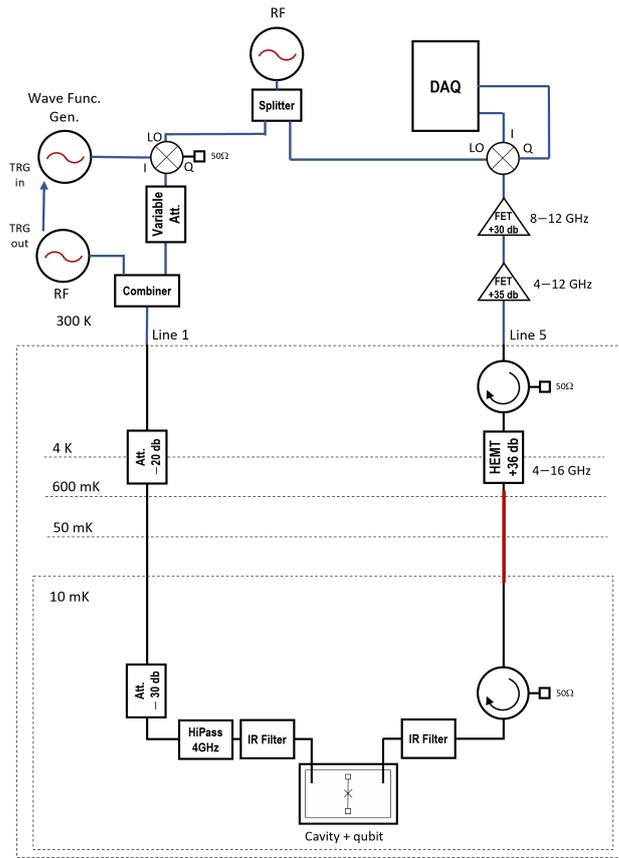
Figure 2. Scheme of the experimental setup used for the transmon characterization.

3. Results

3.1. Transmon Spectroscopic Characterization

The transmon characterization consists in the extraction of the Hamiltonian parameters from the experimental data. The Hamiltonian of a disperesively coupled transmon resonator system (with $\hbar = 1$) is [18]:

$$H_{JC} = (\omega_r - \frac{\chi_{12}}{2} + \chi\sigma^z)a^\dagger a + \frac{1}{2}(\omega_q + \chi_{01})\sigma^z, \tag{1}$$

where ω_r is the resonator angular frequency, σ^z is the Pauli matrix, $a^\dagger$ (a) is the creation (annihilation) operator, and ω_q is the qubit angular frequency. χ is the total dispersive shift which is defined as:

$$\chi = \chi_{01} - \frac{\chi_{12}}{2} \tag{2}$$

while $\chi_{n,n+1}$ are defined as:

$$\chi_{n,n+1} = \frac{g_{n,n+1}^2}{\Delta_{n,n+1}} \tag{3}$$

where $g_{n,n+1}$ is the coupling strength between the energy level n and $n+1$ of the qubit, and $\Delta_{n,n+1}$ is defined as $\omega_{n,n+1} - \omega_r$. $\omega_{n,n+1}$ is the qubit $|n\rangle \rightarrow |n+1\rangle$ transition frequency. In this notation, $\omega_q = \omega_{01}$. Among the different parameters of interest, g_{01}, χ_{01}, χ_{12}, χ, and the anharmonicity α are of particular relevance.

Figure 3 reports the resonator absorption spectrum (S21) acquired as a function of the probing power. Two features are clearly observable, with one appearing at low power and one appearing at high power. The low-power feature accounts for the frequency of the dressed system when the transmon is in the ground state. The sharp high power peak appearing around -75 dbm is given by the bare resonator frequency [26]. For the Al cavity

without the silicon chip, we measure a Q_0 of 217,000 $\pm$ 16,000. These two features of Figure 3 are separated by

$$\omega_r - \omega_r' = \chi + \frac{\chi_{12}}{2}, \tag{4}$$

where ω_r is the bare resonator frequency, while ω_r' is the frequency of the dressed resonator-qubit system. From our data, we obtain that $(\chi + \frac{\chi_{12}}{2})/2\pi = -10.2 \pm 0.1$ MHz.
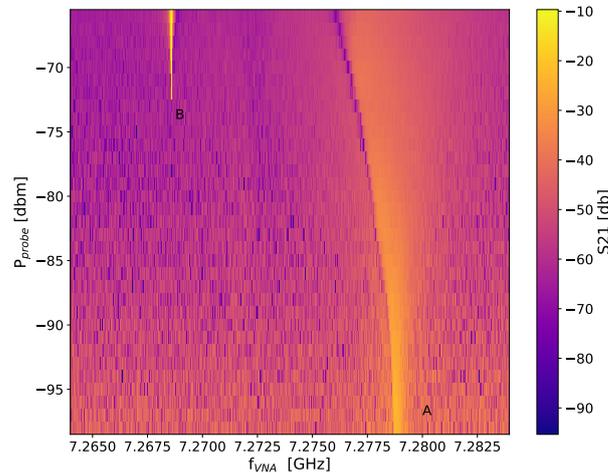
Figure 3. Cavity power scan. The high power feature (B) corresponds to the bare cavity transmission peak. The low power feature (A) is the transmission peak of the dressed cavity-qubit system with the qubit in the ground state.

This power scan of the resonator is an extremely useful preliminary measurement and allows for choosing the most suitable readout power for the qubit characterization in the time domain.

We performed two-tone qubit spectroscopy in order to resolve single photon number peaks inside the cavity [27]. The cavity is coherently probed with a tone resonant with $\omega_r/2\pi = \nu_r$. At the same time with a second tone, we excite the $|0\rangle \rightarrow |1\rangle$ qubit transition. The qubit state and the photon number inside the cavity are coupled (see Equation (1)). Thus, every time the qubit is excited, the cavity absorption peak undergoes a dispersive shift. We detect this as a dip in the cavity absorption spectrum. The qubit absorption spectra acquired for different powers of the cavity probe tone are reported in Figure 4.
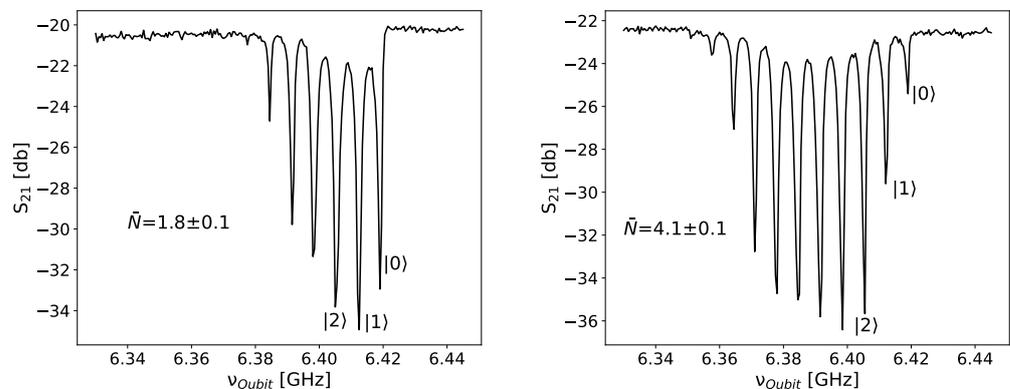
Figure 4. Qubit spectroscopy of individually resolved photon numbers inside the cavity, for an average photon population of $\bar{N} = 1.8$ (**left**, $P_{probe} = -102$ dbm) and $\bar{N} = 4.1$ (**right**, $P_{probe} = -98$ dbm). Each peak is separated by $2\chi/2\pi = -6.82 \pm 0.16$ MHz.

The peaks corresponding to individual photon number states are clearly observable and are separated by $2\chi/2\pi = -6.82 \pm 0.16$ MHz. Combining χ with Equation (4), we

estimate $\chi_{12}/2\pi = -13.6 \pm 0.3$ MHz. Using (2), we obtain that $\chi_{01}/2\pi = -10.2 \pm 0.2$ MHz. We then extract the bare resonance of the qubit. The frequency position of the peak corresponding to zero photons in the cavity is equal to $(\omega_{01} + \chi_{01})/2\pi = 6.4194$ GHz. We obtain $\omega_{01}/2\pi = \nu_{01} = 6.4296$ GHz and hence $\Delta_{01}/2\pi = \nu_{01} - \nu_r = -839$ MHz. We calculate the coupling g_{01}, considering Equation (3) for $n = 0$ obtaining $g_{01}/2\pi = 92.5 \pm 1$ MHz. Since $g_{12} = \sqrt{2}g_{01}$ [18], using Equation (3) with $n = 1$, we can calculate $\Delta_{12}/2\pi = -1260 \pm 40$ MHz. We extract the system anharmonicity as $(\Delta_{01} - \Delta_{12})/2\pi = \nu_{01} - \nu_{12} = \alpha = 421 \pm 84$ MHz. At this point it is straightforward to calculate the capacitance of the transmon inverting [18]:

$$h\alpha = E_c = \frac{e^2}{2C} \tag{5}$$

where h is the Planck constant, E_c is the charging energy, e is the electron charge, and C is the capacitance. We obtain $C = 46 \pm 5$ fF. From the charging energy, we estimate the critical current of the Josephson junction using [18]:

$$\hbar\omega_{01} = \sqrt{8E_c E_J} \tag{6}$$

This couples with a Josephson energy $E_J = \Phi_0 I_c/2\pi$. The value obtained by inverting is $I_c = 24.7$ nA and a Josephson inductane $L_J = \Phi_0/(2\pi I_c) = 13$ nH. The Hamiltonian parameters extracted by the analysis of the experimental data are in good agreement with the output values of the electromagnetic simulation of the qubit-resonator system (see Section 4). We used ANSYS 2023 R1 software to simulate the qubit-resonator coupling factor $g_{01}/2\pi$ and the qubit capacitance. We obtain $g_{01}^{sim}/2\pi = 97$ MHz and $C^{sim} = 57$ fF. A collection of the experimental parameters reported in this and the following section is reported in Table 1.

Table 1. Summary of the experimental qubit-resonator parameters.

Variables	Values
$\chi/2\pi$ [MHz]	-3.41 ± 0.08
$\chi_{01}/2\pi$ [MHz]	-10.2 ± 0.2
$\chi_{12}/2\pi$ [MHz]	-13.6 ± 0.3
α [MHz]	421 ± 84
$g_{01}/2\pi$ [MHz]	$92.5 \pm 1; 75 \pm 12$
C [fF]	46 ± 5
T_1 [µs]	8.68 ± 0.72
T_2 [µs]	2.30 ± 0.11
T_ϕ [µs]	2.65 ± 0.15
L_J [nH]	13 ± 2
I_C [nA]	24.7 ± 1.3

3.2. Time Domain Transmon Characterization

The time domain qubit characterization is conducted using the setup described in Section 2.2. We performed Rabi and Ramsey spectroscopy to measure the relaxation time T_1 and the decoherence time T_2.

Figure 5 reports the Chevron plot for the Rabi frequency, while panel c shows the Rabi oscillations dependence from the excitation pulse power in the on-resonance case. Rabi spectroscopy is essential in studying the time domain behavior of the qubit. This technique allows for determining the temporal length of the excitation pulse that brings the qubit from $|0\rangle$ to $|1\rangle$ (π pulse) or into a superposition state ($\pi/2$ pulse), where $|0\rangle$ and $|1\rangle$ contribute equally. Panel c of Figure 5 reports the power dependence of the Rabi oscillations.
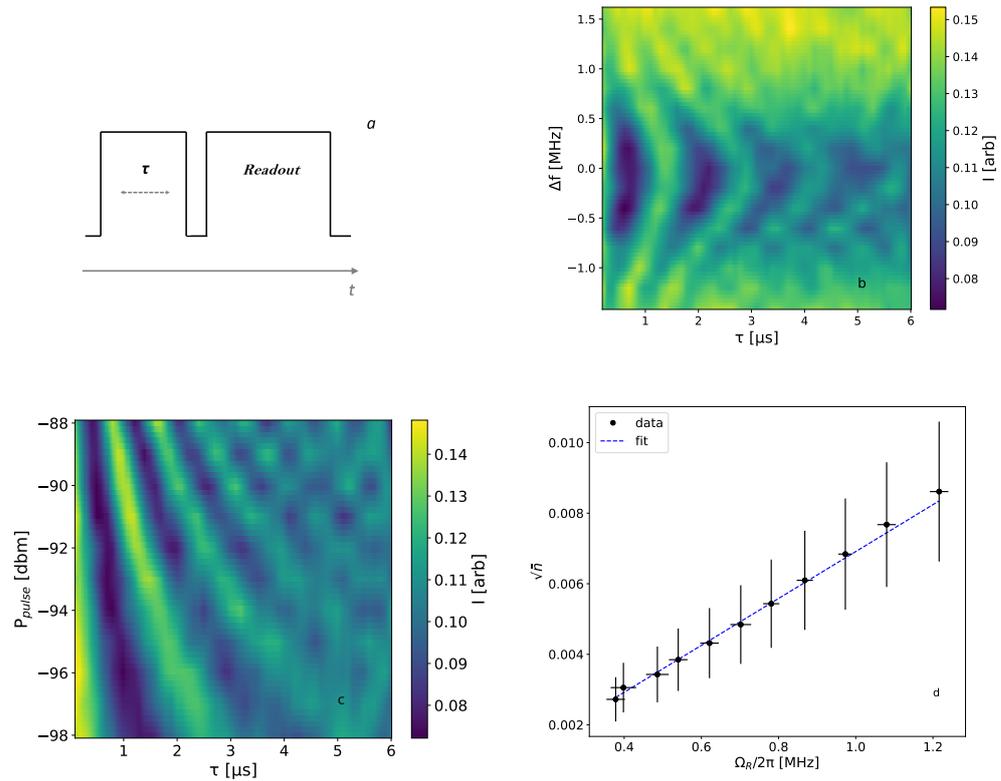
Figure 5. (**a**) measurement scheme for the Rabi spectroscopy. (**b**) Chevron plot, acquired with excitation power P = −93 dbm. The y-axis is given as detuning from the resonance frequency of 6.4194 GHz. (**c**) Rabi oscillation dependence from the excitation tone power. Excitation frequency = 6.4194 GHz. (**d**) Linear dependence of the Rabi frequency from the square root of the average photon number. The data have been fit with a straight line angular coefficient 6.6×10^{-3} MHz^{-1} and intercept 2.6×10^{-4} MHz^{-1}.

From this map, we extract the Rabi frequency dependence from the excitation power (Figure 5d). Adopting the semi-classical approach of [28], where the excitation field is treated as classical, the Rabi frequency dependence from the average number of photons $\bar{n}$ is:

$$\Omega_R = 2g_{01}\sqrt{\bar{n}} \tag{7}$$

By fitting the data of Figure 5d with a straight line, we obtain an independent estimation of $g_{01}/2\pi = 75 \pm 12$ MHz, which is in relatively good agreement with our previous result of 92.5 MHz. We calculated the power entering the cavity in dBm as the sum of the excitation power (generator output power plus the line attenuation) and an additional attenuation factor due to the detuning from the excitation frequency and the resonator frequency. We estimate the latter from simulations to be −104 dB. The excitation power is then converted into watts and we calculate the average number of photons as:

$$\bar{n} = \frac{P}{h\nu\gamma} \tag{8}$$

where P is the excitation power, h is the Planck constant, ν is the excitation frequency, and γ is the cavity dissipation rate, which is estimated to be about 200 kHz from the line width of the low power feature of Figure 3. The large uncertainty value on our $g_{01}/2\pi$ estimation is mainly due to an uncertainty on the power attenuation values that we estimated as ±2 dB.

To extract the qubit lifetime T_1, we measured the ground state population (Figure 6, left). By fitting with an exponential function, we obtain $T_1 = 8.68 \pm 0.72$ μs. We performed Ramsey spectroscopy by sending two off-resonance $\pi/2$ pulses separated by a delay Δt.

Ramsey oscillations of the ground state population are reported in Figure 6 (right panel) for a detuning of 600 KHz. We also reproduced the same measurements with a detuning of 200 and 400 KHz (not shown), and we estimate $T_2 = 2.30 \pm 0.11$ µs. From the T_1 and T_2, we calculate the pure dephasing time T_ϕ through the relation $T_\phi^{-1} = T_2^{-1} - \frac{T_1^{-1}}{2}$. We obtain $T_\phi = 2.65 \pm 0.15$ µs.
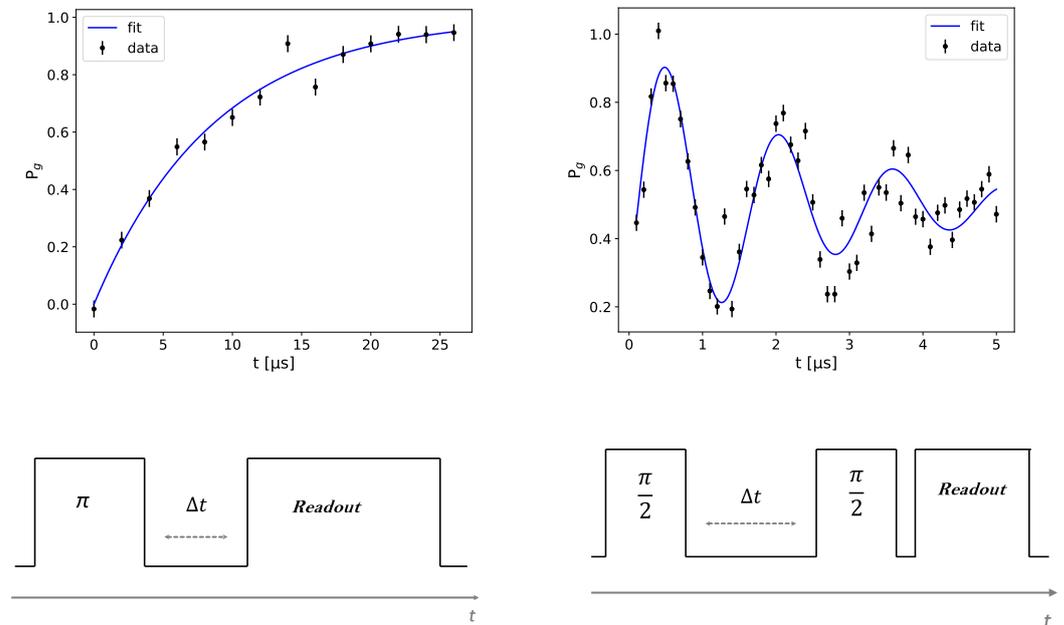
Figure 6. (**Left**): Ground state population (P_g) as a function of the delay time between excitation pulse and qubit readout. $\nu_{excitation} = 6.4194$ GHZ, $P_{excitation} = -93$ dbm. (**Right**): Ramsey spectroscopy, 600 KHz detuned. $\nu_{excitation} = 6.42$ GHZ, $P_{excitation} = -93$ dbm.

4. Simulation

To compare with the experimental results and potentially optimize the design in the future, a simulation of the 3D qubit-resonator system was implemented using Ansys. The model consists of the resonant cavity with the transmon qubit structure on top of the silicon substrate at its center. The properties of the single parts were modeled as follows: silicon substrate as dielectric with relative dielectric constant $\epsilon_s = 11.8$, transmon pads as 2D structure with boundary condition set to superconductor, the Josephson junction as a lumped LC, $L_j = 10$ nH and $C_j = 0.8$ fF, and the cavity as 3D rectangular structure with perfect conductivity as the boundary conditions and vacuum inside. The simulated design in Ansys HFSS is shown in Figure 7.

Several characteristic parameters of the system can be calculated by the simulation. These include the capacitance of the transmon C, the cavity-transmon dipole coupling strength g_{01}, and the lifetime T_1 (Most calculations could be performed directly in Ansys using the fields calculator tool [29]). The values are shown in Table 2.

Table 2. Simulated qubit-resonator parameters

Variables	Values
P_{tot}	4.4×10^{-4}
$T_{purcell}$ [µs]	156
T_{int} [µs]	57
T_1 [µs]	42
C_{tot} [fF]	56
$g_{01}/2\pi$ [MHz]	97
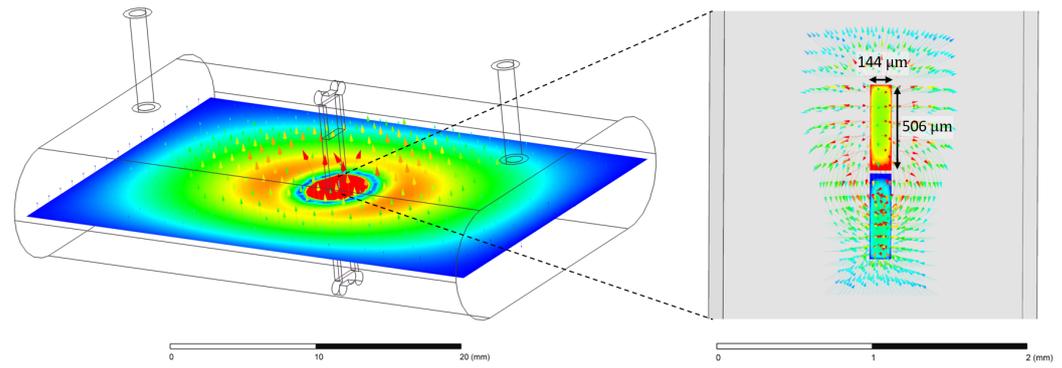
Figure 7. (**Left**): Model in Ansys HFSS of the resonance cavity with the transmon qubit at its center. The TE110 cavity mode, which is influenced by the transmon, is also shown. (**Right**): Zoom in on the transmon with its charge distribution and the local electric field.

4.1. Capacitance

The capacitance of the transmon is calculated from the Maxwell capacitance matrix C^M which is obtained from the ANSYS-Q3D extraction tool. A schematic of the capacitance network of the device is shown in Figure 8. The components of the 2×2 matrix are given by:

$$C_{12} = C_{21} = C_{\text{pads}}, \qquad C_{11} = C_{\text{up}} + C_{\text{pads}}, \qquad C_{22} = C_{\text{down}} + C_{\text{pads}}. \tag{9}$$

The C_{up} and C_{down} are the capacitances between the single pads and an infinite ground plane while C_{pads} is the capacity between the two pads. The effective total capacity for the transmon is (The derivation can be found in the Appendix C):

$$C = \frac{C_{11}C_{22} - C_{12}C_{21}}{C_{11} + C_{12} + C_{21} + C_{22}}. \tag{10}$$

4.2. Dipole Coupling

The coupling strength for the $|0\rangle \rightarrow |1\rangle$ transition is given by [18,30]

$$g_{01} = \frac{2e \cdot d_{eff} \cdot E_0}{\hbar} \frac{1}{\sqrt{2}} \left(\frac{E_j}{8E_c} \right)^{\frac{1}{4}}. \tag{11}$$

where e is the charge of the electron, $\hbar$ is Planck's constant, E_0 is the field amplitude of the cavity mode, E_j is the Josephson energy, and E_c is the charging energy of the transmon:

$$E_0 = \sqrt{\frac{\hbar \omega_r}{2\varepsilon_0 V_{\text{mode}}}}, \qquad E_j = \frac{\Phi_0 I_c}{2\pi}, \qquad E_c = \frac{e^2}{2C}, \tag{12}$$

with ω_r being the resonance frequency of the qubit, the vacuum permittivity ϵ_0, the mode volume V_{mode}, the magnetic flux quantum Φ_0, and the critical current of the junction I_c. V_{mode} is calculated as:

$$V_{\text{mode}} = \frac{\int_V \epsilon_r(\vec{r})|E(\vec{r})|^2 d\vec{r}}{max(|E(\vec{r})|^2)} \tag{13}$$

The effective distance is given by [30]:

$$d_{\text{eff}} = \int_{A_{\text{up}}} \left(\frac{\rho_{up}(\vec{r})}{|q|} \right) \cdot z \, d\vec{r} + \int_{A_{\text{down}}} \left(\frac{\rho_{down}(\vec{r})}{|q|} \right) \cdot z \, d\vec{r} \tag{14}$$

it is calculated in ANSYS-HFSS from the charge distribution $\rho(\vec{r}) = \rho_{up}(\vec{r}) + \rho_{down}(\vec{r})$ on the transmon pads, as shown in Figure 8. A_{up} and A_{down} are the areas of the upper and lower pads. For the electric field, we only considered the fundamental cavity mode TE110.
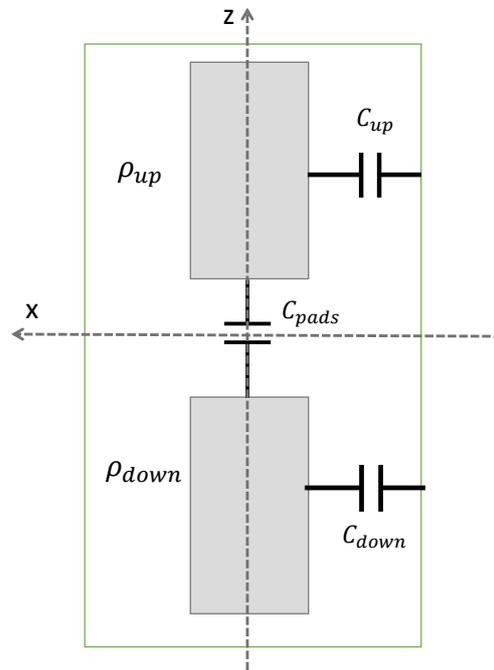
Figure 8. Scheme of the capacitances and the charge density distribution of the transmon qubit. The two rectangles represent the upper pad (**up**) and the bottom pad (**down**) of the qubit. The charge of the pads is $q_{up} = -q_{down} = q$ for the symmetry of the system, with a charge distribution $\rho(\vec{r}) = \rho_{up}(\vec{r}) + \rho_{down}(\vec{r})$. The green rectangle represents an infinite ground plane. The capacitances between the pads and this plane are C_{up} and C_{down}, while the capacitance between the two pads is C_{pads}.

4.3. Relaxation Time T_1

Spontaneous relaxation of the qubit from the excited state to the ground state has a lifetime T_1 to which contribute two main phenomena: losses in the dielectric media around the qubit, (corresponding to an intrinsic lifetime T_{int}), and losses via a coupling to the cavity (corresponding to a lifetime $T_{purcell}$):

$$T_1^{-1} = T_{int}^{-1} + T_{purcell}^{-1} \tag{15}$$

The losses over the cavity due to the Purcell effect are given by [18]:

$$T_{purcell} = \frac{\Delta^2}{g_{01}^2 \kappa} \tag{16}$$

where $\Delta = |\omega_r - \omega_q|$ is the difference in resonance frequency of the cavity and qubit and $\kappa = \omega_r/2Q_{cav}$ is the decay rate of the resonator where Q_{cav} is the quality factor of the cavity.

The dielectric losses can be described in terms of an intrinsic quality factor $Q_{int} = \omega_q T_1^{int}$ of the transmon with contributions from different spatial regions i such as the silicon substrate and the layers of oxide on the surfaces [31]:

$$Q_{int}^{-1} = \sum_i P_i tan(\delta_i). \tag{17}$$

where P_i are the participation ratios and $tan(\delta_i)$ are the material-specific loss tangents. Due to a much larger loss tangent of the surface oxide layers compared to the silicon substrate and aluminium [31], only the surface layers were considered in our analysis. As

they are only about 5 nm thick, the electric field can be approximated to be constant over their thickness.

The participating ratios are therefore given by:

$$P_i = \frac{\epsilon_0 \epsilon_i}{2W} \int_{A_i} d\vec{r} \, \tau_i |E(\vec{r})|^2 = \frac{\epsilon_0 \epsilon_i \tau_i C_{tot}}{q^2} \int_{A_i} d\vec{r} \, |E(\vec{r})|^2 \tag{18}$$

where ϵ_i are the dielectric constants, τ_i is the thickness of the layer, and A_i is the layer surface. The participation ratio is normalized by the total capacitor energy $W = \frac{q^2}{2C_{tot}}$. The $E(\vec{r})$ is the electric field on the surface A_i that is the sum of a parallel and a perpendicular component $E(\vec{r})^2 = E(\vec{r})_\parallel^2 + E(\vec{r})_\perp^2$.

The surface layers considered are the metal-air (MA), metal-substrate (MS), and substrate-air (SA). The following contributions can be derived [32] (Aluminium oxide: $\varepsilon_{MS} = \varepsilon_{MA} = 9.8$ Silicon dioxide: $\varepsilon_{SA} = 3.8$ Silicon substrate: $\varepsilon_S = 11.8$ Loss tangent: $\delta_i = 0.002$ Thickness: $t_i = 5$ nm. The value of the ϵ_i are standard and taken from [31], the loss tangent is taken from [32], and the value of the thickness is an approximation):

$$P_{MS} = \frac{\epsilon_0 \epsilon_S^2}{\epsilon_{MS}} t_{MS} \frac{C_{tot}}{q^2} \int_{MS} d\vec{r} \, |E_{S\perp}|^2 \tag{19}$$

$$P_{MA} = \frac{\epsilon_0}{\epsilon_{MA}} t_{MA} \frac{C_{tot}}{q^2} \int_{MA} d\vec{r} \, |E_{0\perp}|^2 \tag{20}$$

$$P_{SA} = \epsilon_0 t_{SA} \frac{C_{tot}}{q^2} (\epsilon_{SA} \int_{SA} d\vec{r} \, |E_{0\parallel}|^2 + \epsilon_{SA}^{-1} \int_{SA} d\vec{r} \, |E_{0\perp}|^2) \tag{21}$$

where E_0 is the electric field in the air and E_S is the electric field in the substrate while considering the dielectric constant of air as $\epsilon = \epsilon_0$. To calculate these contributions, we used the boundary conditions of the electric field for the perpendicular and parallel components at the interface:

$$E_{1\parallel} = E_{2\parallel} \tag{22}$$

$$\epsilon_1 E_{1\perp} = \epsilon_2 E_{2\perp} \tag{23}$$

with one and two representing the two materials that constitute the interface. As a good approximation, for the MS and MA only the perpendicular contribution is considered and for the SA only the parallel contribution is considered. The detailed derivation can be found in the supplementary materials of [32]. The simulated participation ratios are extracted by using the ANSYS HFSS Field Calculator. An overview of the simulated results is given in Table 2.

While the simulated values of the capacitance and coupling constant align well with the experimental results presented in Table 1, the value for the simulated lifetime of $T_1^{sim} = 42$ μs differs substantially from the experimentally determined value of $T_1^{exp} = 8.68$ μs. This error might originate from an underestimation of the participation ratios due to limitations in our numerical mesh resolution. The large range of scale from millimeters for the pads and nanometers for the edge regions makes it computationally challenging to resolve the electric field accurately, especially in the edge regions where the fields diverge. Previous reports on this have been given in [31,33], wherein also potential solutions are proposed that we are currently exploring.
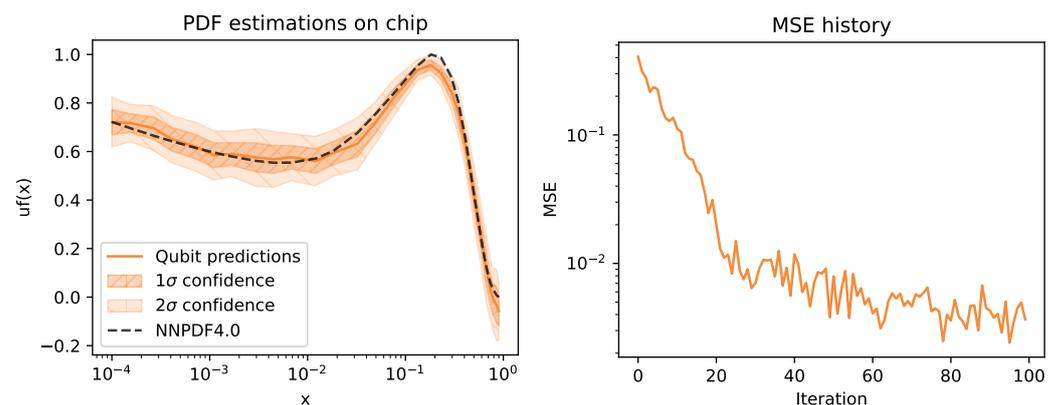
5. Fit to the *u*-Quark Parton Distribution Function of the Proton with a Superconducting Transmon Qubit in a 3D Cavity

With the single-qubit superconducting device presented above, we performed a Quantum Machine Learning application at the Quantum Research Center of the Technology Innovation Institute in Abu Dhabi. It consists of a High Energy Physics application where we train a Parametrized Quantum Circuit (PQC) [34] to fit the *u*-quark Parton Distribution

Function of the proton. The selected PQC has been proved to be effective in [35], wherein a series of simulation tests were carried out. Here, we adopt a similar approach but optimize the model via a hardware-compatible Adam descent [36]. This goal is particularly challenging in terms of execution time, since each optimization step requires the gradient of a loss function with respect to all of the model parameters. When approached on chip using parameter-shift rules [37–39], the calculation involves the execution of a number of circuits proportional to the number of parameters of the model we are training.

In the context of Quantum Machine Learning (QML) [40,41], the `Qibo` framework, with its modular structure, is exploited to develop and test pure quantum full-stack algorithms [42–45]. `Qibo` [46,47] is a full stack open-source middleware framework for quantum computing. The `Qibo` suite includes full-state vector simulators, which have been shown to be compatible with the state-of-the-art [48,49] and several tools dedicated to quantum control and quantum calibration [50,51]. Quantum control is implemented through a dedicated backend, `Qibolab`, able to provide control over a different set of electronics including Radio Frequency Systems on Chip (RFSoC) [52]. `Qibolab` [53] also provides primitives to compile and transpile quantum circuits. The calibration and characterization of QPUs is delegated to `Qibocal` [54], a `Qibo` module which includes several pre-coded experiments necessary to fine-tune calibration parameters, reporting tools, and methods to automatically update QPU parameters. In this particular setup, the qubit is controlled with a RFSoC 4×2 through `Qibolab` and the calibration was performed using `Qibocal`.

We target the u-quark Parton Distribution Function (PDF) using the NNPDF4.0 grid [55] as reference, applying a z-score normalization to the target values $\text{PDF}(x) \equiv uf(x)$ for each considered momentum fraction x to constrain them in the range $[0, 1]$, which is of particular interest since our QML predictions are computed as the expected value of a Non-Interacting Pauli Z. A summary of the obtained results and of the selected hyperparameters is reported in Table 3. In Figure 9, we show the final predictions of the trained model. Each targeted PDF value $uf(x_i)$ is computed $N_{\text{runs}} = 50$ times and the collected results $\{uf(x_i)^k\}_{k=1}^{N_{\text{runs}}}$ are used to calculate the estimations and their uncertainties as averages $\langle uf(x_i)^k \rangle_k$ and standard deviations $\langle uf(x_i)^k - \langle uf(x_i)^k \rangle_k \rangle_k$ over the N_{runs} predictions (We use the superscript k to describe the k-th prediction of the PDF for a fixed momentum value x_i, represented by the subscript i. We also use the notation $\langle y^k \rangle_k \equiv \frac{1}{N} \sum_{k=1}^{N} y_k$ to describe the average of the N variables).

Figure 9. (**Left**), fit of the u-quark Parton Distribution Function values performed using a Variational Quantum Circuit trained with gradient descent on a self-hosted single-qubit superconducting device. The estimation of the PDF value for each point is calculated as the average of $N_{\text{runs}} = 50$ predictions computed using the trained qubit. The uncertainty intervals are computed instead using one (dark orange) and two (light orange) standard deviations from the mean considering the same N_{runs} predicted values. (**Right**), Mean Squared Error (MSE) values as function of the optimization iterations.

Table 3. Summary of hyper-parameters and results of the performed QML algorithm.

Parameter	N_{train}	N_{params}	Optimizer	N_{shots}	MSE_{final}	Inst.	T_{exe}
Value	30	14	Adam	250	3.6×10^{-3}	ZCU111	$78'$

6. Measurement Protocol for a Low Dark-Count Photon Detector with Two Qubits

It is notable that 3D resonators can reach extremely high quality factors and it has been demonstrated that they can store a microwave photon for a time of up to 10^{-2} s at mK temperature [23]. Coupling a high performance 3D resonator with a qubit can enable applications like quantum memories and single photon detection. Several experimental schemes for a single photon detector based on qubit-resonator coupling have been proposed [6–10]. We propose here an extension of the method described in [6] that aims at reducing the dark counts. Our approach is based on a system where two qubits with different resonant frequencies are dispersively coupled to the same resonator. In this configuration, the two qubits can be addressed separately and the qubit-qubit crosstalk is suppressed as long as the qubits have resonant frequencies that are different on the order of about 100 MHz [56].

The Jaynes–Cummings Hamiltonian of two qubits dispersively coupled to the same resonator mode is [28,57]:

$$H_{JC} = [\omega_r + \chi(\sigma_1^z + \sigma_2^z)]a^\dagger a + \sum_{i=1}^{2} \frac{\omega_i}{2}\sigma_i^z \tag{24}$$

where the indexes one and two are used to differentiate the qubits and we assumed that the two qubits have the same dispersive shift χ but different frequency $\omega_1 \neq \omega_2$. We also assume that $\chi \gg k$ where k is the resonator width. In (24), we neglected the two qubits state-swap term since $\omega_1 \neq \omega_2$ [28].

We prepare both of the qubits in the state $\frac{1}{\sqrt{2}}(|0\rangle + |1\rangle)$ by rotating around the Y axis of the Bloch sphere of $\pi/2$ from the $|0\rangle$ state. For both qubits, we send control pulses of proper length and power at the frequencies ω_1 and ω_2. The state after initialization is

$$|Q_1 Q_2\rangle = \frac{1}{2}(|0\rangle + |1\rangle) \times (|0\rangle + |1\rangle) \tag{25}$$

We assume that a photon of frequency ω_R is emitted into a coaxial cable terminated on the resonator. At time $T \ll \sqrt{(T_1^2 + T_2^2)/2}$ after the initialization, we send two additional $-\pi/2$ rotation pulses along the Y axis to complete the Ramsey spectroscopy on the two qubits. Since the qubits and the cavity photons are entangled, the total wavefunction has to be written as the product of the photons and qubit wavefunctions. If no photon impinged on the cavity, then the final state is

$$|Q_1 Q_2\rangle_{\overline{\gamma}} = |0\rangle \times |0\rangle \tag{26}$$

If otherwise, a photon indeed reflected on the resonator, and it will gain a different phase according to the reflection coefficient in Equation (A17) (see Appendix B for the full calculations). Since the resonance frequency of the resonator depends on the states of the two qubits, the photon will acquire a phase $\phi = 0$ if $|Q_1 Q_2\rangle = (|0\rangle \times |1\rangle + |1\rangle \times |0\rangle)/2$, $\phi = \pi$ if $|Q_1 Q_2\rangle = |1\rangle \times |1\rangle$ and $\phi = -\pi$ if $|Q_1 Q_2\rangle = |0\rangle \times |0\rangle$ as shown in Figure 10. We then have

$$\begin{aligned}
|Q_1 Q_2\rangle_\gamma &= \frac{1}{2}\left(e^{-i\pi}|00\rangle + |10\rangle + |01\rangle + e^{i\pi}|11\rangle\right) \\
&= \frac{-1}{2}(|00\rangle - |10\rangle - |01\rangle + |11\rangle) \\
&= -\frac{1}{2}(|0\rangle - |1\rangle) \times (|0\rangle - |1\rangle)
\end{aligned} \tag{27}$$

Therefore, closing the Ramsey cycle with the two $Y^{-\pi/2}$ pulses, we have

$$|Q_1 Q_2\rangle_\gamma = |1\rangle \times |1\rangle \tag{28}$$

Comparing the two states in Equations (26) and (28), we see that when measuring the states of the two qubits independently, the probability to read a $|11\rangle$ state where there was no photon requires a readout error on both qubits, so that the $Rate \sim p_{error}^2$. For the independent readout of the two qubits, we plan to use two separate resonators, each of which is individually coupled to one of the qubits.
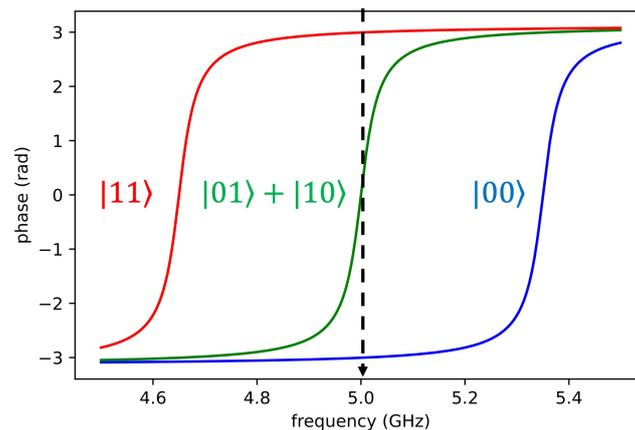
Figure 10. Phase shift for the reflected photon as a function of the state of the qubits. To build this graph, we assumed a resonator frequency of 5 GHz.

7. Conclusions

In this article, we report the fabrication and characterization of a transmon qubit dispersively coupled with a 3D resonator. We show the experimental methods we used to extract the Hamiltonian parameters. Using spectroscopic techniques, we managed to measure the coupling strength g_{01}, the anharmonicity α, the transmon capacity C, and the dispersive shift χ (a complete list can be found in Table 1). We measured the coherence properties of the transmon in the time domain measuring T_1, T_2 and T_ϕ. We also managed to obtain a second estimation of the coupling strength g_{01} by studying the Rabi frequency dependence from the excitation power. The two measured values of $g_{01}/2\pi$, 92.5 ± 1 and 75 ± 12 MHz, are in good agreement. We provide a complete roadmap for simulation in ANSYS to design a transmon with the desired properties, (e.g., coupling strength), starting from the geometry of the system and a few other input parameters. This approach predicts reasonably well the value of the coupling strength for our system g_{01}^{sim} = 97 MHz. With the single-qubit device, we performed a Quantum Machine Learning application where we train a Parametrized Quantum Circuit to fit the u-quark Parton Distribution Function of the proton. In the final part of the article, we propose a two qubits-based microwave photon counter for the realization of which we underline the importance of possessing the tools necessary for the design, fabrication, and characterization of qubits.

Author Contributions: Conceptualization, S.C.; Data curation, A.D., S.C., A.P. and C.G.; Formal analysis, A.D. and C.G.; Funding acquisition, S.C., A.G. and C.G.; Investigation, A.D., M.B., F.C., D.D.G., C.L., G.M., L.P., A.R., S.T. and C.G.; Methodology, L.B., S.C., A.G. and C.G.; Project administration, C.G.; Resources, B.A., A.A., F.R. and C.G.; Software, A.D., S.C., F.H., M.M., E.P., M.R. and S.T.; Supervision, C.G.; Validation, C.G.; Visualization, A.D., F.H., E.P., A.P., A.R. and M.R.; Writing—original draft, A.D., B.A., A.A., S.C., F.H., A.S.P.K., E.P., A.R., M.R. and C.G.; Writing—review and editing, A.D. and C.G. All authors have read and agreed to the published version of the manuscript.

Appendix A. Average Photon Number inside the Cavity

From the qubit absorption spectra reported in Figure 4, it is possible to extract the average number of photons inside the cavity as a consequence of the readout process. The qubit absorption spectra reflect the coherent photon distribution inside the cavity. As a consequence, the intensity of each peak expressed as a function of the relative Fock state number must follow a Poisson distribution [27]:

$$P(n) = A \frac{e^{-\bar{N}}}{n!} \tag{A1}$$

where A is an arbitrary scale factor, n is the cavity Fock state number, and $\bar{N}$ is the average photon number inside the cavity. Fitting the intensity distributions of the absorption peaks reported in Figure 4, we managed to extract the average number of photons inside the cavity, which are $\bar{N} = 1.8 \pm 0.1$ ($P_{probe} = -102$ dBm) and $\bar{N} = 4.1 \pm 0.1$ ($P_{probe} = -98$ dBm).
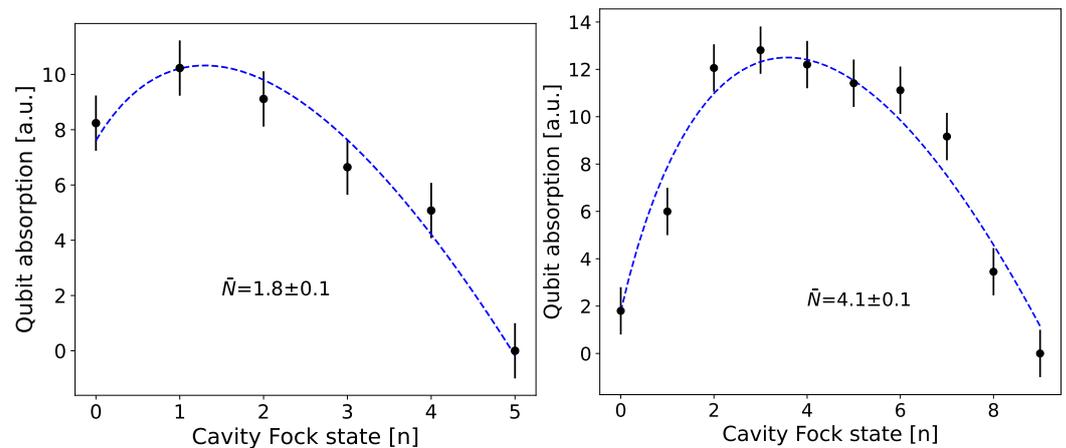
Figure A1. Qubit absorption spectra peaks intensity distribution extracted from the data reported in Figure 4 as a function of the Fock state number. Left, $P_{probe} = -103$ dbm, right, $P_{probe} = -98$ dbm. The black dots are the experimental data, the broken line is a fit performed using a Poisson distribution. The y axis is in logarithmic scale.

Appendix B. Quantum Treatment of LC+Transmission Line

Following Yurke and Denker [58] we start from the lagrangian density of a transmission line, with unit lenght capacitance C_l and inductance L_l, coupled to a parallel LC:

$$\mathcal{L} = \left(\frac{C_l}{2} \dot{\phi}^2 - \frac{1}{2L_l} \phi'^2 \right) \sigma(x) \tag{A2}$$
$$+ \left(\frac{C}{2} \dot{\phi}^2 - \frac{1}{2L} \phi^2 \right) \delta(x)$$

where ϕ is the flux variable. The Lagrange equations are:

$$\frac{d}{dt}\frac{\partial\mathcal{L}(x,t)}{\partial\dot{q}} + \frac{d}{dx}\frac{\partial\mathcal{L}(x,t)}{\partial q'} = \frac{\partial\mathcal{L}(x,t)}{\partial q} \tag{A3}$$

We obtain

$$\left(C_l\ddot{\phi} - \frac{1}{L_l}\phi''\right)\sigma(x) + \left[-\frac{1}{L_l}\phi' + C\ddot{\phi} + \frac{\phi}{L}\right]\delta(x) = 0$$

The conjugate momentum is

$$\Pi = \frac{d\mathcal{L}}{d\dot{\phi}} = C_l\dot{\phi}\sigma(x) + C\dot{\phi}\delta(x) = Q(x,t)\sigma(x) + Q_0(t)\delta(x) \tag{A4}$$

and the commutation relations is

$$\left[\phi(x,t),\Pi(x',t)\right] = i\hbar\delta(x-x')$$

note that in $x = x' = 0$ $[\phi, C\dot{\phi}] = i\hbar$. Note also that $Q(x,t)$ is a charge density while Q_0 is a charge.

Since $\phi(x,t)$ is a solution of the wave equation, it is of the form

$$\phi(x,t) = \phi^{out}(\omega t - kx) + \phi^{in}(\omega t + kx)$$

so that

$$\phi' = \frac{1}{v}(\dot{\phi}^{in} - \dot{\phi}^{out}) = \frac{1}{v}(2\dot{\phi}^{in} - \dot{\phi})$$

and we can write the equation of motion in $x = 0$ as

$$C\ddot{\phi} + \frac{\phi}{L} + \frac{1}{Z_0}\dot{\phi} = 2\frac{1}{Z_0}\dot{\phi}^{in} \tag{A5}$$

where we used the relation $vL_l = Z_0$ the TL characteristic impedance.

For $x > 0$ we find a solution of the form

$$\phi(x,t) = \int_{-\infty}^{\infty} dk N_k[a(k)\exp\{[-i(\omega_k t - kx)]\} + a(k)^\dagger \exp\{[+i(\omega_k t - kx)]\}] \tag{A6}$$

and the conjugate momentum

$$Q(x,t) = C_l\dot{\phi}(x,t) = C_l\int_{-\infty}^{\infty} dk N_k(-i\omega)[a(k)\exp\{[-i(\omega_k t - kx)]\} \tag{A7}$$
$$-a(k)^\dagger\exp\{[+i(\omega_k t - kx)]\}]$$

by inverting these relations

$$a(k) = \frac{1}{4\pi N_k}\exp\{(i\omega_k t)\}\int_{-\infty}^{+\infty} dx\exp\{(-ikx)\}\left(\phi(x,t) + \frac{i}{C_l\omega_k}Q(x,t)\right) \tag{A8}$$
$$a^\dagger(k) = \frac{1}{4\pi N_k}\exp\{(-i\omega_k t)\}\int_{-\infty}^{+\infty} dx\exp\{(ikx)\}\left(\phi(x,t) - \frac{i}{C_l\omega_k}Q(x,t)\right)$$

Then we have:

$$[a(k), a^\dagger(q)] = \delta(k-q) \tag{A9}$$

provided that

$$N_k = \sqrt{\frac{\hbar}{4\pi C_l\omega_k}} \tag{A10}$$

Then we have

$$\phi(x,t) = \sqrt{\frac{\hbar}{4\pi C_l}} \int_{-\infty}^{\infty} \frac{dk}{\sqrt{\omega_k}} [a(k) \exp\{[-i(\omega_k t - kx)]\} + a(k)^\dagger \exp\{[+i(\omega_k t - kx)]\}] \tag{A11}$$

and the conjugate momentum

$$Q(x,t) = -i\sqrt{\frac{\hbar C_l}{4\pi}} \int_{-\infty}^{\infty} dk \sqrt{\omega_k} [a(k) \exp\{[-i(\omega_k t - kx)]\} - a(k)^\dagger \exp\{[+i(\omega_k t - kx)]\}] \tag{A12}$$

Changing variable and using the relation between vector momentum and frequency $|k|v = \omega$

$$\begin{aligned}
\phi(x,t) &= \sqrt{\frac{\hbar}{4\pi C_l v}} \int_0^\infty \frac{d\omega}{\sqrt{\omega}} [\frac{a(k)}{\sqrt{v}} \exp\{-i(\omega t - kx)\} \\
&\quad + \frac{a(-k)}{\sqrt{v}} \exp\{-i(\omega t + kx)\}] + h.c. \\
Q(x,t) &= -i\sqrt{\frac{\hbar C_l}{4\pi v}} \int_0^\infty d\omega \sqrt{\omega} [\frac{a(k)}{\sqrt{v}} \exp\{[-i(\omega t - kx)]\} \\
&\quad + \frac{a(-k)}{\sqrt{v}} \exp\{[-i(\omega t + kx)]\}] + h.c.
\end{aligned}$$

$$\begin{aligned}
\phi(x,t) &= \sqrt{\frac{\hbar Z_0}{4\pi}} \int_0^\infty \frac{d\omega}{\sqrt{\omega}} [a^{out}(\omega) \exp\{[-i(\omega t - kx)]\} \\
&\quad + a^{in}(\omega) \exp\{[-i(\omega t + kx)]\}] + h.c. \\
Q(x,t) &= -i\sqrt{\frac{\hbar}{4\pi Z_0}} \frac{1}{v} \int_0^\infty d\omega \sqrt{\omega} [a^{out}(\omega) \exp\{[-i(\omega t - kx)]\} \\
&\quad + a^{in}(\omega) \exp\{[-i(\omega t + kx)]\}] + h.c.
\end{aligned}$$

where $a^{out} = a(k)/\sqrt{v}$ and $a^{in} = a(-k)/\sqrt{v}$ and

$$[a^\alpha(\omega), a^{\alpha'\dagger}(\omega')] = \delta_{\alpha,\alpha'}\delta(\omega - \omega') \tag{A13}$$

in $x = 0$

$$\begin{aligned}
\phi(0,t) &= \sqrt{\frac{\hbar Z_0}{4\pi}} \int_0^\infty \frac{d\omega}{\sqrt{\omega}} \exp\{(-i\omega t)\} [a^{out}(\omega) + a^{in}(\omega)] + h.c. = \tag{A14} \\
&= \sqrt{\frac{\hbar Z_R}{2}} (b + b^\dagger) \\
Q_0(t) &= C\dot{\phi} = -i\sqrt{\frac{\hbar Z_0}{4\pi}} C \int_0^\infty d\omega \sqrt{\omega} \exp\{(-i\omega t)\} [a^{out}(\omega) + a^{in}(\omega)] + h.c. \\
&= -i\sqrt{\frac{\hbar}{2Z_R}} (b - b^\dagger)
\end{aligned}$$

where

$$b(t) = \sqrt{\frac{Z_0}{2\pi Z_R}} \int_0^\infty \frac{d\omega}{\sqrt{\omega}} \exp\{(-i\omega t)\} a(\omega) \tag{A15}$$

and $Z_R = \sqrt{L/C}$ and $\omega_R = 1/\sqrt{LC}$ are the proper impedance and frequency of the LC resonator.

Replacing (A14) in Equation (A5)

$$a(\omega) = 2i\frac{Z_j\omega_j}{Z_0}a^{in}(\omega)\frac{\omega}{\omega^2 - \omega_R^2 + i\omega\omega_j Z_R/Z_0} \tag{A16}$$

the Fourier transform is $a(t) \sim a(\omega_R)\exp\{(-\omega_R Z_R/2Z_0 t)\}$ so that there is a damping rate in energy, considering a factor 2 for the square amplitude, $\gamma = \omega_R Z_R/Z_0 = \omega_R/Q$, where $Q = Z_0/Z_R$. The reflection coefficient is obtained substituting $a(\omega) = a^{in}(\omega) + a^{out}(\omega)$

$$\Gamma = \frac{a^{out}(\omega)}{a^{in}(\omega)} = -\frac{\omega^2 - \omega_R^2 - i\omega\omega_R Z_R/Z_0}{\omega^2 - \omega_R^2 + i\omega\omega_R Z_R/Z_0} \tag{A17}$$

The module of the reflection coefficient is always equal to 1 while the phase moves from $-\pi$ to $+\pi$ crossing the resonance frequency of the resonator as shown in Figure A2.
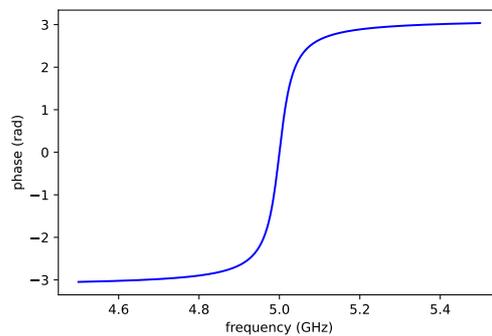

Figure A2. Phase as a function of frequency

Appendix C. Capacitance Matrix and Total Capacitance

The system's total capacity is given by (10). The formula can be derived starting from the Maxwell capacity matrix

$$C^M = \begin{bmatrix} C_{11} & C_{12} \\ C_{21} & C_{22} \end{bmatrix}. \tag{A18}$$

The relation between the charge and the potential is $\mathbf{Q} = \mathbf{C^M V}$:

$$\begin{bmatrix} Q_1 \\ Q_2 \end{bmatrix} = \begin{bmatrix} C_{11} & C_{12} \\ C_{21} & C_{22} \end{bmatrix}\begin{bmatrix} V_1 \\ V_2 \end{bmatrix}, \tag{A19}$$

where Q_1 and Q_2 are the charges of the pad up and pad down respectively and V_1 and V_2 are the corresponding charge potentials. Defining the inverse matrix $\mathbf{E} = (\mathbf{C^M})^{-1}$, the relation become:

$$\begin{bmatrix} V_1 \\ V_2 \end{bmatrix} = \begin{bmatrix} E_{11} & E_{12} \\ E_{21} & E_{22} \end{bmatrix}\begin{bmatrix} Q_1 \\ Q_2 \end{bmatrix} \tag{A20}$$

with the corresponding equation:

$$\begin{cases} V_1 = E_{11}Q_1 + E_{12}Q_2 \\ V_2 = E_{21}Q_1 + E_{22}Q_2 \end{cases}. \tag{A21}$$

The voltage difference between the pads is:

$$\Delta V = V_1 - V_2 = (E_{11} - E_{12} + E_{22} - E_{21})Q \tag{A22}$$

considering $Q = Q_1 = -Q_2$ due to the symmetry of the system. The current flowing between the pads is given by $I = -\frac{dQ}{dt}$, therefore $\frac{dI}{dt} = -\frac{d^2Q}{dt^2}$. Considering a linear inductance L between the pads, the voltage is:

$$\Delta V = L\frac{d^2Q}{dt^2} \tag{A23}$$

Combining (A22) and (A23), results in

$$\frac{d^2Q}{dt^2} = \frac{E_{11} - E_{12} + E_{22} - E_{21}}{L}Q \tag{A24}$$

As the transmon in the first approximation is an LC harmonic oscillator we can compare it with (A24) and see that

$$C = (E_{11} - E_{12} + E_{22} - E_{21})^{-1} \tag{A25}$$

The formula (A25) can be written depending on the components of the Maxwell capacity matrix $\mathbf{C^M}$, obtaining the relation for the capacity:

$$C = \frac{C_{11}C_{22} - C_{12}C_{21}}{C_{11} + C_{12} + C_{21} + C_{22}} \tag{A26}$$

References

1. Preskill, J. Quantum computing and the entanglement frontier. *arXiv* **2012**, arXiv:1203.5813.
2. Kjaergaard, M.; Schwartz, M.E.; Braumüller, J.; Krantz, P.; Wang, J.I.J.; Gustavsson, S.; Oliver, W.D. Superconducting qubits: Current state of play. *Annu. Rev. Condens. Matter Phys.* **2020**, *11*, 369–395. [CrossRef]
3. D'Elia, A.; Rettaroli, A.; Tocci, S.; Babusci, D.; Barone, C.; Beretta, M.; Buonomo, B.; Chiarello, F.; Chikhi, N.; Di Gioacchino, D.; et al. Stepping closer to pulsed single microwave photon detectors for axions search. *IEEE Trans. Appl. Supercond.* **2022**, *33*, 1–9. [CrossRef]
4. Rettaroli, A.; Alesini, D.; Babusci, D.; Barone, C.; Buonomo, B.; Beretta, M.M.; Castellano, G.; Chiarello, F.; Di Gioacchino, D.; Felici, G.; et al. Josephson junctions as single microwave photon counters: Simulation and characterization. *Instruments* **2021**, *5*, 25. [CrossRef]
5. Golubev, D.S.; Il'ichev, E.V.; Kuzmin, L.S. Single-photon detection with a Josephson junction coupled to a resonator. *Phys. Rev. Appl.* **2021**, *16*, 014025. [CrossRef]
6. Kono, S.; Koshino, K.; Tabuchi, Y.; Noguchi, A.; Nakamura, Y. Quantum non-demolition detection of an itinerant microwave photon. *Nat. Phys.* **2018**, *14*, 546–549. [CrossRef]
7. Besse, J.C.; Gasparinetti, S.; Collodo, M.C.; Walter, T.; Kurpiers, P.; Pechal, M.; Eichler, C.; Wallraff, A. Single-Shot Quantum Nondemolition Detection of Individual Itinerant Microwave Photons. *Phys. Rev. X* **2018**, *8*, 021003. [CrossRef]
8. Inomata, K.; Lin, Z.; Koshino, K.; Oliver, W.D.; Tsai, J.S.; Yamamoto, T.; Nakamura, Y. Single microwave-photon detector using an artificial Λ-type three-level system. *Nat. Commun.* **2016**, *7*, 12303. [CrossRef]
9. Dixit, A.V.; Chakram, S.; He, K.; Agrawal, A.; Naik, R.K.; Schuster, D.I.; Chou, A. Searching for Dark Matter with a Superconducting Qubit. *Phys. Rev. Lett.* **2021**, *126*, 141302. [CrossRef]
10. Lescanne, R.; Deléglise, S.; Albertinale, E.; Réglade, U.; Capelle, T.; Ivanov, E.; Jacqmin, T.; Leghtas, Z.; Flurin, E. Irreversible Qubit-Photon Coupling for the Detection of Itinerant Microwave Photons. *Phys. Rev. X* **2020**, *10*, 021038. [CrossRef]
11. Butseraen, G.; Ranadive, A.; Aparicio, N.; Rafsanjani Amin, K.; Juyal, A.; Esposito, M.; Watanabe, K.; Taniguchi, T.; Roch, N.; Lefloch, F.; et al. A gate-tunable graphene Josephson parametric amplifier. *Nat. Nanotechnol.* **2022**, *17*, 1153–1158. [CrossRef] [PubMed]
12. Aumentado, J. Superconducting parametric amplifiers: The state of the art in Josephson parametric amplifiers. *IEEE Microw. Mag.* **2020**, *21*, 45–59. [CrossRef]
13. Macklin, C.; O'brien, K.; Hover, D.; Schwartz, M.; Bolkhovsky, V.; Zhang, X.; Oliver, W.; Siddiqi, I. A near–quantum-limited Josephson traveling-wave parametric amplifier. *Science* **2015**, *350*, 307–310. [CrossRef] [PubMed]
14. D'Elia, A.; Rettaroli, A.; Chiarello, F.; Di Gioacchino, D.; Enrico, E.; Fasolo, L.; Ligi, C.; Maccarrone, G.; Mantegazzini, F.; Margesin, B.; et al. Microwave Photon Emission in Superconducting Circuits. *Instruments* **2023**, *7*, 36. [CrossRef]
15. Peugeot, A.; Ménard, G.; Dambach, S.; Westig, M.; Kubala, B.; Mukharsky, Y.; Altimiras, C.; Joyez, P.; Vion, D.; Roche, P.; et al. Generating two continuous entangled microwave beams using a dc-biased Josephson junction. *Phys. Rev. X* **2021**, *11*, 031008. [CrossRef]

16. Esposito, M.; Ranadive, A.; Planat, L.; Leger, S.; Fraudet, D.; Jouanny, V.; Buisson, O.; Guichard, W.; Naud, C.; Aumentado, J.; et al. Observation of two-mode squeezing in a traveling wave parametric amplifier. *Phys. Rev. Lett.* **2022**, *128*, 153603. [CrossRef] [PubMed]

17. Martinis, J.M. Superconducting phase qubits. *Quantum Inf. Process.* **2009**, *8*, 81–103. [CrossRef]

18. Koch, J.; Terri, M.Y.; Gambetta, J.; Houck, A.A.; Schuster, D.I.; Majer, J.; Blais, A.; Devoret, M.H.; Girvin, S.M.; Schoelkopf, R.J. Charge-insensitive qubit design derived from the Cooper pair box. *Phys. Rev. A* **2007**, *76*, 042319. [CrossRef]

19. Wang, C.; Li, X.; Xu, H.; Li, Z.; Wang, J.; Yang, Z.; Mi, Z.; Liang, X.; Su, T.; Yang, C.; et al. Towards practical quantum computers: Transmon qubit with a lifetime approaching 0.5 milliseconds. *npj Quantum Inf.* **2022**, *8*, 3. [CrossRef]

20. Hyyppä, E.; Kundu, S.; Chan, C.F.; Gunyhó, A.; Hotari, J.; Janzso, D.; Juliusson, K.; Kiuru, O.; Kotilahti, J.; Landra, A.; et al. Unimon qubit. *Nat. Commun.* **2022**, *13*, 6895. [CrossRef]

21. Gyenis, A.; Mundada, P.S.; Di Paolo, A.; Hazard, T.M.; You, X.; Schuster, D.I.; Koch, J.; Blais, A.; Houck, A.A. Experimental realization of a protected superconducting circuit derived from the 0–π qubit. *PRX Quantum* **2021**, *2*, 010339. [CrossRef]

22. Bao, F.; Deng, H.; Ding, D.; Gao, R.; Gao, X.; Huang, C.; Jiang, X.; Ku, H.S.; Li, Z.; Ma, X.; et al. Fluxonium: An alternative qubit platform for high-fidelity operations. *Phys. Rev. Lett.* **2022**, *129*, 010502. [CrossRef] [PubMed]

23. Reagor, M.; Paik, H.; Catelani, G.; Sun, L.; Axline, C.; Holland, E.; Pop, I.M.; Masluk, N.A.; Brecht, T.; Frunzio, L.; et al. Reaching 10 ms single photon lifetimes for superconducting aluminum cavities. *App. Phys. Lett.* **2013**, *102*, 192604. [CrossRef]

24. Somoroff, A.; Ficheux, Q.; Mencia, R.A.; Xiong, H.; Kuzmin, R.; Manucharyan, V.E. Millisecond Coherence in a Superconducting Qubit. *Phys. Rev. Lett.* **2023**, *130*, 267001. [CrossRef] [PubMed]

25. Joshi, A.; Noh, K.; Gao, Y.Y. Quantum information processing with bosonic qubits in circuit QED. *Quantum Sci. Technol.* **2021**, *6*, 033001. [CrossRef]

26. Gao, Y.Y.; Rol, M.A.; Touzard, S.; Wang, C. Practical guide for building superconducting quantum devices. *PRX Quantum* **2021**, *2*, 040202. [CrossRef]

27. Schuster, D.; Houck, A.A.; Schreier, J.; Wallraff, A.; Gambetta, J.; Blais, A.; Frunzio, L.; Majer, J.; Johnson, B.; Devoret, M.; et al. Resolving photon number states in a superconducting circuit. *Nature* **2007**, *445*, 515–518. [CrossRef] [PubMed]

28. Blais, A.; Gambetta, J.; Wallraff, A.; Schuster, D.I.; Girvin, S.M.; Devoret, M.H.; Schoelkopf, R.J. Quantum-information processing with circuit quantum electrodynamics. *Phys. Rev. A* **2007**, *75*, 032329. [CrossRef]

29. ANSYS, Inc. *HFSS Fields Calculator Cookbook*; Release 17.0; ANSYS, Inc.: Canonsburg, PA, USA, 2015.

30. Miller, S. *A Tunable 20 GHz Transmon Qubit in a 3D Cavity*; Swiss Federal Institute of Technology Zurich: Zurich, Switzerland, 2018.

31. Martinis, J.M. Surface loss calculations and design of a superconducting transmon qubit with tapered wiring. *npj Quantum Inf.* **2022**, *8*, 26. [CrossRef]

32. Wenner, J.; Barends, R.; Bialczak, R.C.; Chen, Y.; Kelly, J.; Lucero, E.; Mariantoni, M.; Megrant, A.; O'Malley, P.J.J.; Sank, D.; et al. Surface loss simulations of superconducting coplanar waveguide resonators. *Appl. Phys. Lett.* **2011**, *99*, 113507. [CrossRef]

33. Wang, C.; Axline, C.; Gao, Y.Y.; Brecht, T.; Chu, Y.; Frunzio, L.; Devoret, M.H.; Schoelkopf, R.J. Surface participation and dielectric loss in superconducting qubits. *Appl. Phys. Lett.* **2015**, *107*, 162601, [CrossRef]

34. Cerezo, M.; Arrasmith, A.; Babbush, R.; Benjamin, S.C.; Endo, S.; Fujii, K.; McClean, J.R.; Mitarai, K.; Yuan, X.; Cincio, L.; et al. Variational quantum algorithms. *Nat. Rev. Phys.* **2021**, *3*, 625–644. [CrossRef]

35. Pérez-Salinas, A.; Cruz-Martinez, J.; Alhajri, A.A.; Carrazza, S. Determining the proton content with a quantum computer. *Phys. Rev. D* **2021**, *103*, 034027. [CrossRef]

36. Kingma, D.P.; Ba, J. Adam: A Method for Stochastic Optimization. *arXiv* **2017**, arXiv:1412.6980.

37. Mitarai, K.; Negoro, M.; Kitagawa, M.; Fujii, K. Quantum circuit learning. *Phys. Rev. A* **2018**, *98*, 032309. [CrossRef]

38. Schuld, M.; Bergholm, V.; Gogolin, C.; Izaac, J.; Killoran, N. Evaluating analytic gradients on quantum hardware. *Phys. Rev. A* **2019**, *99*, 032331. [CrossRef]

39. Mari, A.; Bromley, T.R.; Killoran, N. Estimating the gradient and higher-order derivatives on quantum hardware. *Phys. Rev. A* **2021**, *103*, 012405. [CrossRef]

40. Schuld, M.; Sinayskiy, I.; Petruccione, F. An introduction to quantum machine learning. *Contemp. Phys.* **2014**, *56*, 172–185. [CrossRef]

41. Biamonte, J.; Wittek, P.; Pancotti, N.; Rebentrost, P.; Wiebe, N.; Lloyd, S. Quantum machine learning. *Nature* **2017**, *549*, 195–202. [CrossRef]

42. Robbiati, M.; Efthymiou, S.; Pasquale, A.; Carrazza, S. A quantum analytical Adam descent through parameter shift rule using Qibo. *arXiv* **2022**, arXiv:2210.10787.

43. Robbiati, M.; Cruz-Martinez, J.M.; Carrazza, S. Determining probability density functions with adiabatic quantum computing. *arXiv* **2023**, arXiv:2303.11346.

44. Cruz-Martinez, J.M.; Robbiati, M.; Carrazza, S. Multi-variable integration with a variational quantum circuit. *arXiv* **2023**, arXiv:2308.05657.

45. Robbiati, M.; Sopena, A.; Papaluca, A.; Carrazza, S. Real-time error mitigation for variational optimization on quantum hardware. *arXiv* **2023**, arXiv:2311.05680.

46. Efthymiou, S.; Ramos-Calderer, S.; Bravo-Prieto, C.; Pérez-Salinas, A.; García-Martín, D.; Garcia-Saez, A.; Latorre, J.I.; Carrazza, S. Qibo: A framework for quantum simulation with hardware acceleration. *Quantum Sci. Technol.* **2021**, *7*, 015018. [CrossRef]

47. Efthymiou, S.; Ramos-Calderer, S.; Bravo-Prieto, C.; Pérez-Salinas, A.; García-Martín, D.; Garcia-Saez, A.; Latorre, J.I.; Carrazza, S. Quantum-TII/qibo: Qibo. *Zenodo* **2020**. [CrossRef]

48. Efthymiou, S.; Lazzarin, M.; Pasquale, A.; Carrazza, S. Quantum simulation with just-in-time compilation. *Quantum* **2022**, *6*, 814. [CrossRef]

49. Efthymiou, S.; Carrazza, S.; Pasquale, A.; Mello, R.; Lazzarin, M.; Sopena, A.; Pedicillo, E.; vodovozovaliza. qiboteam/qibojit: qibojit 0.1.0. *Zenodo* **2023**. [CrossRef]

50. Efthymiou, S.; Orgaz-Fuertes, A.; Carobene, R.; Cereijo, J.; Pasquale, A.; Ramos-Calderer, S.; Bordoni, S.; Fuentes-Ruiz, D.; Candido, A.; Pedicillo, E.; et al. Qibolab: An open-source hybrid quantum operating system. *arXiv* **2023**, arXiv:2308.06313.

51. Pasquale, A.; Efthymiou, S.; Ramos-Calderer, S.; Wilkens, J.; Roth, I.; Carrazza, S. Towards an open-source framework to perform quantum calibration and characterization. *arXiv* **2023**, arXiv:2303.10397.

52. Carobene, R.; Candido, A.; Serrano, J.; Orgaz-Fuertes, A.; Giachero, A.; Carrazza, S. Qibosoq: An open-source framework for quantum circuit RFSoC programming. *arXiv* **2023**, arXiv:2310.05851.

53. Efthymiou, S.; Orgaz, Á.; Carobene, R.; Cereijo, J.; Carrazza, S.; Pasquale, A.; Simone-Bordoni; Sarlle, D.; Pedicillo, E.; maxhant; et al. qiboteam/qibolab: Qibolab 0.1.2. *Zenodo* **2023**. [CrossRef]

54. Pasquale, A.; Pedicillo, E.; Sarlle, D.; Efthymiou, S.; Cereijo, J.; Carrazza, S.; Vodovozovaliza; Orgaz, Á.; Sopena, A.; Candido, A.; et al. qiboteam/qibocal: Qibocal 0.0.4. *Zenodo* **2023**. [CrossRef]

55. Ball, R.D.; Carrazza, S.; Cruz-Martinez, J.; Debbio, L.D.; Forte, S.; Giani, T.; Iranipour, S.; Kassabov, Z.; Latorre, J.I.; Nocera, E.R.; et al. The path to proton structure at 1% accuracy. *Eur. Phys. J. C* **2022**, *82*, 428. [CrossRef]

56. Majer, J.; Chow, J.; Gambetta, J.; Koch, J.; Johnson, B.; Schreier, J.; Frunzio, L.; Schuster, D.; Houck, A.A.; Wallraff, A.; et al. Coupling superconducting qubits via a cavity bus. *Nature* **2007**, *449*, 443–447. [CrossRef]

57. Blais, A.; Huang, R.S.; Wallraff, A.; Girvin, S.M.; Schoelkopf, R.J. Cavity quantum electrodynamics for superconducting electrical circuits: An architecture for quantum computation. *Phys. Rev. A* **2004**, *69*, 062320. [CrossRef]

58. Yurke, B.; Denker, J.S. Quantum network theory. *Phys. Rev. A* **1984**, *29*, 1419. [CrossRef]